

Staggered Fibrils and Damageable Interfaces Lead Concurrently and Independently to Hysteretic Energy Absorption and Inhomogeneous Strain Fields in Cyclically Loaded Antler Bone

P. De Falco,[†] E. Barbieri,[†] N. Pugno,^{†,‡,§} and H. S. Gupta^{*,†,‡}

[†]School of Engineering and Material Science, Queen Mary University of London, London E1 4NS, United Kingdom

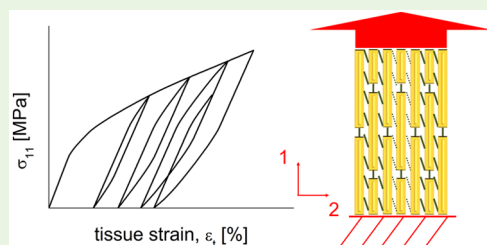
[‡]Laboratory of Bio-Inspired and Graphene Nanomechanics, Department of Civil, Environmental and Mechanical Engineering, University of Trento, Trento 38122, Italy

[§]Center for Materials and Microsystems, Fondazione Bruno Kessler, Povo, Trento 38122, Italy

Supporting Information

ABSTRACT: The high toughness and work to fracture of hierarchical composites, like antler bone, involve structural mechanisms at the molecular, nano-, and micro scales, which are not completely explored. A key characteristic of the high energy absorption of such materials is the large hysteresis during cyclic loading, but its origin remains unknown. In situ synchrotron X-ray diffraction tests during tensile loading of antler bone showed heterogeneous fibrillar deformation and hysteresis. To explain the origin of these mechanisms from the nanostructure of antler bone, here we develop a class of finite-element fibril models whose predictions are compared to experimental data across a range of potential composite architectures. We demonstrate that the key structural motif enabling a match to experimental data is an axially staggered arrangement of stiff mineralized collagen fibrils coupled with weak, damageable interfibrillar interfaces.

KEYWORDS: antler bone, interface, nanoscale, cohesive behaviors, heterogeneity, hysteresis



1. INTRODUCTION

Natural structural materials exhibit mechanical properties through complex hierarchical architectures and load-absorbing mechanisms. These architectures evolved naturally from basic building blocks thanks to a “self-organization” strategy during growth.¹ In fact, biological structures adapt, change function during growth, renew their material, and build hierarchies.² The macroscopic behavior of these materials depends on the interaction between structural properties at different scales.³ Biocomposites, such as bone, shells and nacre, represent an excellent example of how the design at lower hierarchical scales confers higher mechanical properties than the single constituents.⁴ Although the stiffness of these biocomposites is comparable to that of the basic constituent at the nanoscale, their toughness results hugely increased. For instance, in bone and shell, the toughness of the mineral constituents is $\ll 1$ MPa $m^{1/2}$, whereas the toughness of their macrostructure varies, respectively, in a range of 2–7 MPa $m^{1/2}$ and 3–7 MPa $m^{1/2}$.

Bone, as shown in Figure 1, at the nanometer scale length is a composite of stiff inorganic hydroxyapatite platelets interleaved with a softer organic matrix, made principally of type I tropocollagen proteins.⁵ This substructure, together with an intrafibrillar phase of noncollagenous proteins and mineral, forms mineralized fibrils that are arranged into aggregate structures at higher levels and larger length scales, such as fibril arrays and lamellae.¹ The structural aspects of this architecture served as inspiration for bioinspired materials that replicate the

nanometre scale fibril-matrix^{6–10} and intrafibrillar¹¹ structure, or at micrometer scales.^{12,13} Nonetheless, the mechanical interactions between the constituent units and the higher length scales remain a matter of active research. In particular, previous studies focused on how the hierarchical architecture brings functionally desirable properties such as high toughness,¹⁴ energy absorption, and fatigue resistance.¹⁵

At the range of 1–100 μm , accepted and validated toughness mechanisms are crack deflection and bridging,¹⁶ and constrained microcracking.¹⁷ The nanoscale structure is believed to be of fundamental importance for bone toughness. However, it is both challenging to investigate experimentally¹⁸ as well as to explain the reasons of its mechanical properties at this scale with a model. Works to date mainly focused on either deformation beyond the yield point under uniaxial or localized loading^{18–20} or on posthoc interpretation of electron microscopic images of loaded and fractured bone.^{21,22} These experimental studies led to hypothesize different toughness mechanisms.²³ Examples include intrafibrillar plasticity,²⁰ sacrificial bonds within noncollagenous proteins,²² friction

Special Issue: Multiscale Biological Materials and Systems: Integration of Experiment, Modeling, and Theory

Received: October 17, 2016

Accepted: December 19, 2016

Published: December 19, 2016

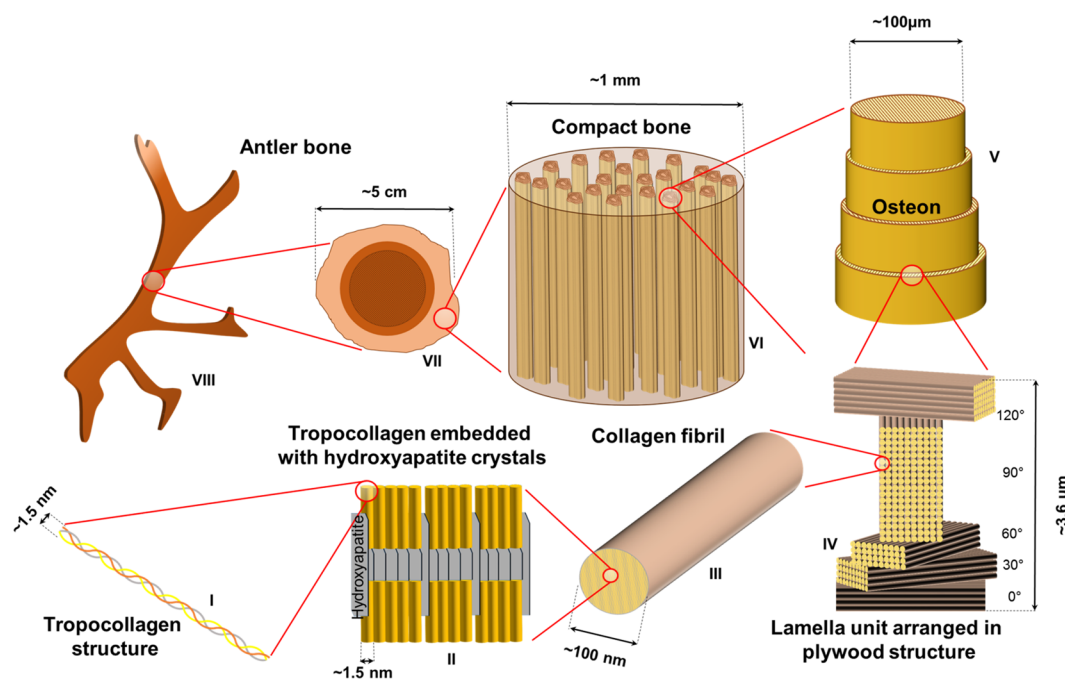


Figure 1. Hierarchical structure in antler bone: The collagen fibrils (II) are made of tropocollagen molecule (I) and hydroxyapatite mineral. At the following hierarchical level, these fibrils are wrapped in a protein-based matrix (III) forming a plywood structure: the lamella unit (IV). This group is repeated in the osteon (V), which is part of the compact bone (VI), and therefore of the antler bone structure (VII–VIII).

between collagen and mineral,²⁴ fibrillar sliding of mineralized collagen fibrils,²⁵ interfibrillar sliding of collagen fiber arrays²⁶ and microcracking.²⁷ At these small length scales, relatively less clear evidence exists on the response to cyclic loading, although recent experimental work has begun to shed light on this question. For example, Schwiedrzik et al.²⁸ focused on compression and cyclic micropillar tests on lamellar bone and measured axial and transverse apparent moduli and compressive strengths.

Bone is physiologically subjected to external periodic loading that can lead to fatigue failure, and high rate impact that instead can lead to fracture. It is then of considerable interest to understand how the nanostructure behaves under these loading conditions. Unfortunately, experimental information on the structural changes at the fibrillar and interfibrillar level in these loading modes is relatively scarce. Concurrently, the link between the types of fibrillar architecture and the developed cyclic inelastic response is also not very clear. In this regard, a recurrent generic motif in the architecture of hard biological composites is a staggered arrangement of fibrils (Figure 2b).²⁹ This particular arrangement plays a key role in energy dissipation through sliding^{30,31} and in enhancing the structural elastic properties.^{32,33} Gupta et al.²⁰ identified elastoplastic behavior for the individual mineralized fibril under the assumption of staggered configuration of mineral platelets and collagen molecules inside the fibril.

The role of such a staggered configuration in cyclic loading and energy absorption is unexplored at the nanoscale. Recent in situ synchrotron SAXD/WAXD mechanical loading/unloading tests on antler bone²⁰ show hysteresis in stress–strain curves at both the macroscopic and the fibrillar level. These results also highlight the presence of two groups of fibrils: plastically deforming fibrils, which exhibit larger deformation (which will be denoted type A in what follows), and elastically deforming fibrils (denoted type B), whose deformation remains at or under the strain at the material yield point. It is clear that these

structural mechanisms may be related, and that the fibrillar hysteresis is an important component of the high work to fracture of antler, but its structural origins are far less understood. In situ experimental probes of the type described above need to be combined with ultrastructural modeling at the scale of 1–100 nm, in order to develop a deeper understanding of the relevant mechanisms.

In this paper, we present a set of finite element simulations of the mineralized fibrils in antler bone under cyclic loading whose results, when matched to experiment, give an understanding of the causes of the fibrillar hysteresis. We will show that the combination of a damageable interface and staggered fibrillar arrangement turns out to be capable of explaining the experimentally observed hysteretic loops in loading/unloading curves. In addition, a clear explanation of the biphasic fibrillar deformation mechanisms, in terms of the dependence on interfacial strength and architecture, is here reported. These results provide new insights of toughening mechanisms at the nanoscale in antler bone.

2. METHODS

2.1. Experimental Method. The preparation description of antler bone specimens and the in situ mechanical tests with synchrotron small-angle X-ray diffraction (SAXD) are described in detail in a previous paper,²⁰ and summarized here briefly. The samples were taken from the antler cortical shell of a red deer (*Cervus elaphus*) near the antler-pedicle junction and tested with SAXD measurements, combined with cyclic loading. While the details are available in our previous papers,³⁴ they will be summarized here for completeness. Figure 2a shows a highly simplified schematic for tensile cyclic tests on hydrated antler bone specimens combined with time-resolved synchrotron SAXD measurements, where a synchrotron X-ray beam impinges on the specimen, leading to a sequence of SAXD patterns acquired as the sample is deformed.

Meridional peaks are visible in the SAXD pattern, due to the periodic electron density profile arising from the axial D-stagger of the tropocollagen molecules inside the fibril ($D \approx 65\text{--}67$ nm for

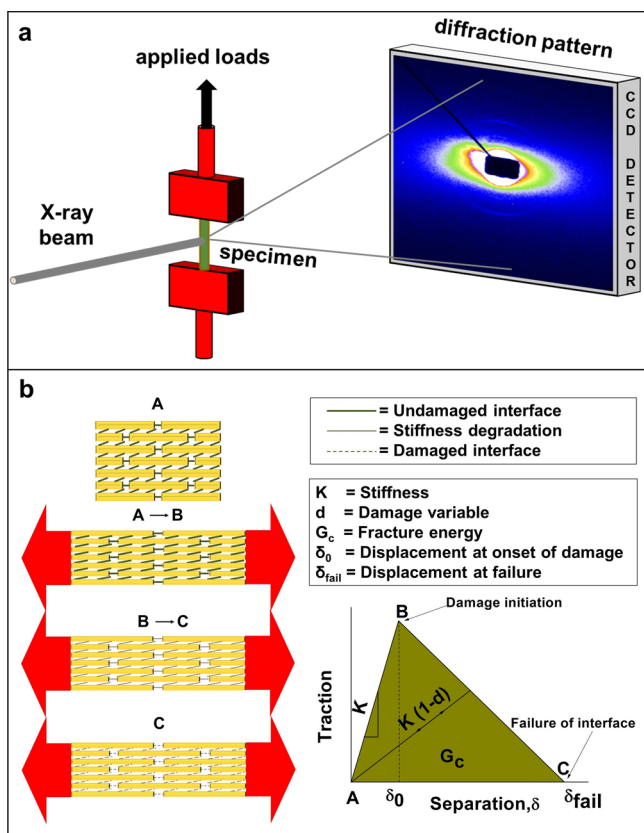


Figure 2. Experimental and numerical methods: (a) Experimental setup in synchrotron. Mechanical tester design for tensile testing. (b) Staggered fibril structure at the scale of 0.1–10 μm with cohesive surface behaviors at the interface. The interfibrillar interface is modeled with a cohesive-traction separation law. A–B, linear stiffness; B, onset of damage; B–C, damage evolution curve characterized by the stiffness degradation coefficient $(1 - d)K$; C, failure of interface.

vertebrate collagenous tissues). Percentage shifts in these peak positions are therefore measures of fibril strain, as reported previously for bone (e.g., Gupta et al.,³⁵ Dong et al.,³⁶ Zimmermann et al.,³⁷ among others). The third order meridional peak was used for determination of mean fibril strain, via the relation $D = 6\pi/q_{03}$ where q_{03} was the peak position, in reciprocal space, of the meridional peak. Further, the peak width w_q was also determined, which (as reported in Krauss et al.³⁴ and Gupta et al.²⁰) provides a measure of the heterogeneity of fibrillar deformation: a narrow w_q corresponds to a uniform fibrillar deformation with all fibrils in the scattering volume deforming similarly, while an increasing w_q corresponds to an increasing heterogeneity, or dispersion, in the fibril strain distribution. As the details are presented in Gupta et al.,²⁰ we note only that by tracking the stress-induced increase in mean fibril strain, together with the increase in w_q , was a biphasic fibrillar deformation observed, and it will serve as part of the comparison of our presented model to experiment.

2.2. Numerical Method and Implementation of the Model.

Parametric finite elements simulations were performed to test a seven-layer staggered fibrillar system using Abaqus (Abaqus 6.14–1, Dassault Systemes). The two-dimensional model is made of 2800 CPS4R finite elements (CPS4R corresponds to 4-node, reduced integration with hourglass control). The plates, measuring $10 \mu\text{m} \times 0.2 \mu\text{m}$, represent the fibrils (with 200 nm or $0.2 \mu\text{m}$ radius²) in bone and are connected through cohesive laws, which are shown in detail in Figure 2b.³⁸ Interfaces link both the lateral sides of fibrils (“mode I interface”) and their bottom-up sides (“mode II interfaces”) (see Figure 3c for interfaces definition). The model (Figure 2b) assumes initially linear elastic behavior (eq 1, next page) followed by the initiation and

evolution of damage. In eq 1, the traction stress vector consists, as our models are two-dimensional, of two components t_n and t_s , which are, respectively, the normal and shear tractions, and δ_n and δ_s which represent the relative displacements between the nodes on the adjacent surfaces of two different fibrils. We decided to use the simplest traction-separation law, where normal (K_{nn}) and tangential (K_{ss}) stiffness are not coupled (K_{ns} and K_{sn} are null in eq 1).

$$t = \begin{bmatrix} t_n \\ t_s \end{bmatrix} = \begin{bmatrix} K_{nn} & 0 \\ 0 & K_{ss} \end{bmatrix} \begin{bmatrix} \delta_n \\ \delta_s \end{bmatrix} \quad (1)$$

As peak traction values for the mode I and mode II undamageable interfaces, we used generic values such as $t_n^0 = t_s^0 = 80 \text{ MPa}$. These values are never achieved among the finite elements adjacent to the interfaces and do not affect the results. For mode II damageable interfaces we adopted the values $t_n^0 = 80 \text{ MPa}$ and $t_s^0 = 0.8 \text{ MPa}$; t_n^0 is an arbitrary high value, never reached upon the structure, whereas t_s^0 is the shear stress occurring when at least one point in the structure reaches yielding. We followed the hypothesis²⁰ that heterogeneity, because of progressive mode II interface damage, starts occurring in correspondence of the yielding point. We imposed this condition by choosing as shear traction peak value, the maximum shear stress, recorded in a generic point of structure, which occurs when at least one finite element reaches the yielding stress prescribed by the material model used for the simulations ($\sigma_y \approx 46 \text{ MPa}$, which is the yield point observed experimentally for antler bone in Gupta et al.²⁰). The damage initiation values t_n^0 and t_s^0 were chosen such that mode I interfaces are never damageable, while the mode II interfaces could be either damageable or not. Therefore, we adopted a maximum stress criterion for the onset of damage (eq 2) where damage initiates when the maximum ratio between the traction values at the interface ($\langle t_n \rangle$, t_s) and the peak values (t_n^0 and t_s^0) reaches the value of one. The symbols $\langle \rangle$ represent the Macaulay brackets that are used to mean that a compressive traction does not initiate the damage.

$$\max \left\{ \frac{\langle t_n \rangle}{t_n^0}, \frac{t_s}{t_s^0} \right\} = 1 \quad (2)$$

We used the values $K_{nn} = K_{ss} = 100 \text{ MPa}$ as stiffness coefficients for both mode I and mode II interfaces. The choice of K_{nn} for the mode II interface and K_{ss} for the mode I interface has no effect on the results. The response of the system was then expected to be mainly affected by K_{nn} for the mode I interface and by K_{ss} for the mode II one. We performed parametric simulations, keeping all the parameters fixed except for K_{nn} for the mode I interface and K_{ss} for the mode II interface. We varied these values between 100 and 300 $\text{MPa}/\mu\text{m}$, with a step of 100 $\text{MPa}/\mu\text{m}$ (in total 9 simulations), and we found that when $K_{nn} = K_{ss} = 100 \text{ MPa}/\mu\text{m}$, the numerical maximum tissue strain matches the correspondent experimental value closely. We chose these coefficients such that both the numerical and the experimental systems achieve the same level of maximum tissue strain. We expressed the coefficients K_{nn} and K_{ss} as K in Figure 2b, as the figure is representative of a generic mode of fracture. The choice of K_{nn} for the mode I interface and K_{ss} for the mode II interface is fundamental for the obtained results; in fact it affects not only the deformation of the system but also the hysteretic width of loops in stress–strain curves.

As displacements at failure of the interfaces, we adopted the arbitrary high values 10 and 3 μm , respectively for the undamageable interfaces and for the damageable interface. These levels of displacement values are never achieved by the finite elements in our simulations, over the course of the stress and strain range seen experimentally, and are hence selected to make sure that the damage occurs only in terms of stiffness degradation and never of complete failure. Specifically, we assumed that the stresses are always transferred through the interfaces. For damageable interfaces, once the damage initiates, the stiffness follows the degradation law: $K' = (1 - d)K$, where $d \in [0, 1]$ is the damageable variable. The total dissipated energy (per unit of area) through the process of damage of the interface is the area under the traction-separation curve (represented

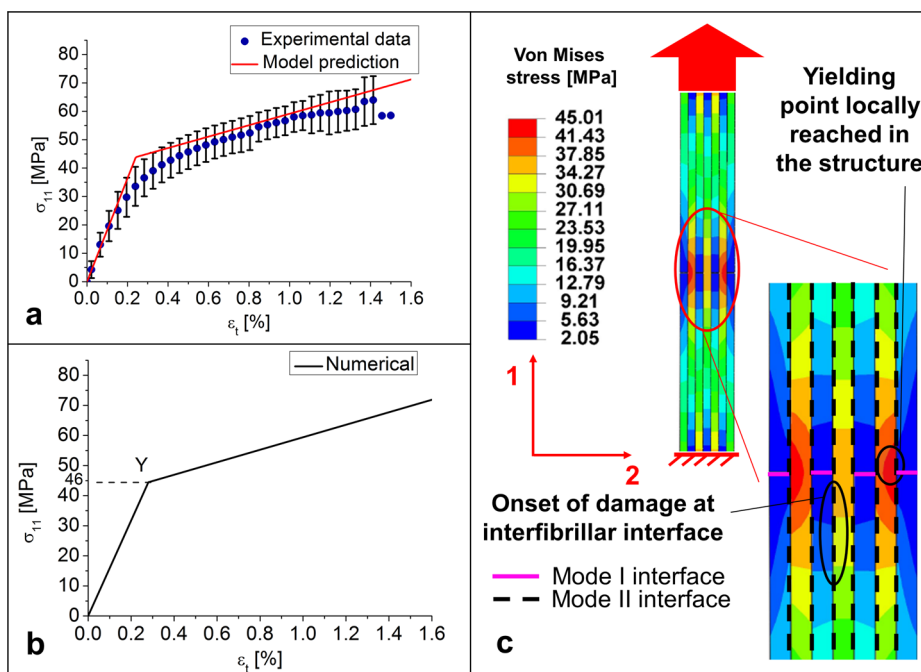


Figure 3. Experimental and numerical fibril stress–strain curves: (a) Experimental stress–strain curve for antler bone versus model prediction. Data are averaged from 10 uniaxial stretch-to-failure tests and bars are standard deviations (data from ref 20). (b) Material properties input for simulations. (c) Cohesive interface characterization. The interface surrounding the central fibril starts damaging when at least one finite element of the whole structure reaches yielding at 46 MPa (maximum stress criterion).

as G_c in Figure 2b). In Table 1 we schematically summarize the values adopted for the cohesive simulations.

Table 1. Input Values for Cohesive Models Used in the FE Analyses^a

	mode I interface	mode II undamageable interface	mode II damageable interface
elastic constant for fracture mode I: K_{nn} (MPa/ μm)	100	100	100
elastic constant for fracture mode II: K_{ss} (MPa/ μm)	100	100	100
peak traction for fracture mode I: t_n^0 (MPa)	80	80	100
peak traction for fracture mode II: t_s^0 (MPa)	80	80	0.8
separation value δ (μm)	10	10	3

^aBold fonts indicate the parameters that critically affect the simulations.

The material properties adopted for the fibrils follow a previous model (Figure 3a),²⁰ with the Young's modulus of 15.8 GPa and the yielding of 46 MPa (Figure 3b). In other words, the elastoplastic behavior of a single fibril, and its yield point and stiffness, are taken as a given, and arise from previous experimental work (Gupta et al.^{20,39}). Tensile and cyclic static simulations were performed to study respectively the biphasic fibrillar deformation (section 3.1) and hysteretic loops in stress–strain curves. The applied loads reproduce the values used for experiments by Gupta et al.²⁰ Uniaxial traction, along the direction 1 (see Figure 3c), was applied to the top end of the finite element models and fixed support to the bottom end, while right and left sides were kept unconstrained. In detail, a traction value of 60 MPa was imposed for the static tests and a sequence of different traction values for the cyclic tests (43–0–50–0–56–0–60–0–43 MPa). The uniaxial tissue strain was computed as ratio between the displacement of the loaded edge and the initial length, not by averaging the strain field. This is because the average of the strains over

the structure does not account for the deformation of the cohesive interfaces. In fact, because cohesive interfaces are essentially springs, small gaps appear between the fibrils (visible, for example, in Figure 4c). These gaps are not cracks, but only representative of relative displacements between fibrils.

3. RESULTS

3.1. Biphasic Fibrillar Deformations. As stated earlier, a main experimental finding in Gupta et al.²⁰ was a biphasic fibrillar deformation. Our aim was to understand the role of cohesive interfibrillar surface interfaces in staggered mineralized fibril models, in enabling this behavior. In this regard the multipanel Figure 4 shows an overview comparing strain distributions between experimental data and numerical simulations. These will be explored in detail below.

For tensile simulations, we first adopted a nondamageable law for both the mode I and the mode II interfaces, shown previously in Figure 3c. The results of applied uniaxial traction on the fibrils are shown in Figure 4d, with relative magnification in Figure 4c, with both fibrils A and B plastically deforming, as expected. The maximum longitudinal stress (σ_{11}), reached in central region of the fibrils, is 135 MPa in fibril A and 119 MPa in fibril B, while the averaged stresses are, respectively, 65 and 63 MPa, beyond the yield point.

Second, we found that the introduction of damageable mode II interface around the middle layer produces a differentiation of the fibril behaviors. The damage of the interface around the middle layer partially “isolates” fibril B, which is then not able to fully contribute to the load absorption. While fibril A remains elastoplastic in its deformation behavior, the deformation of fibril B never exceeds the elastic range (Figures 4c–f). In fact, although the maximum longitudinal stress (σ_{11}), locally measured in a restricted region of fibril B, is 58 MPa (beyond the yield point), its homogenized stress is below the yield point (39 MPa). The corresponding values for fibril A are

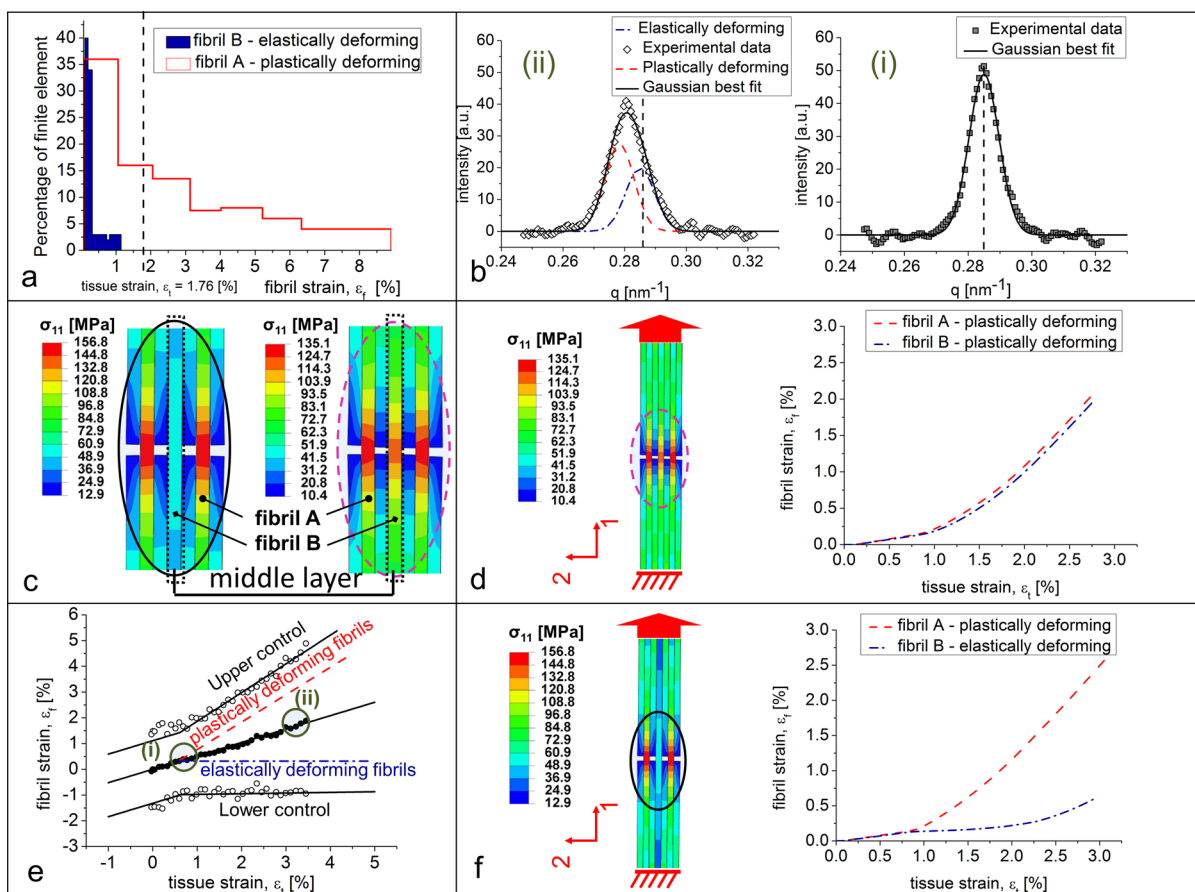


Figure 4. Experimental and numerical fibrillar deformation mechanisms: (a) Strain distribution for elastically and plastically deforming fibrils for a tissue strain value of 1.76%. (b) SAXD intensity plots (data from ref 20). (i) Tissue strain at the yield value of 0.6% (highlighted by a circle and the letter (i) in e). (ii) Tissue strain at the value of 3.2% (highlighted by a circle and the letter (ii) in e). (c) Stress distributions with and without damageable interfaces. Zoom from panels d and f. (d) Fibril behaviors in the presence of undamageable interfaces between fibrils. Fibril b, at the center of the middle layer, deforms plastically. (e) Variation of mean fibril strain (filled circles) and upper and lower control lines plotted against tissue strain (data from ref 20). The middle solid line is the linear regression against tissue strain. (f) Fibril behaviors in the presence of damageable interface only between the middle layer and the adjacent two layers. Fibril b, at the center of the middle layer, deforms elastically.

respectively 157 and 73 MPa. Considering a particular level of macroscopic tissue strain beyond the yield point, such as $\varepsilon_t = 1.76\%$ (Figure 4a), we find that most of the load (86%) is carried by fibril A whose finite elements are able to stretch up to eight times more than the finite elements in fibril B. For this tissue strain value, the largest deformation in fibril A is $\varepsilon_f = 8.9\%$, whereas in fibril B it is $\varepsilon_f = 1.2\%$. In addition, the average deformation of fibril A is 0.9%, whereas for fibril B, the equivalent strain is 0.2% (below the yield point).

In Figure 4f, curves show that numerical results are in good agreement with the experimental results shown in Figure 4e, where a comparison between experimental results and model predictions, developed by Gupta et al.,²⁰ is presented. In particular, the figure includes the upper and lower control lines ($\varepsilon_{f,\pm 25\%}$), the best fit linear regression against tissue strain (middle solid line), and the model predictions for both the elastically deforming fibril (blue dash-dotted line) and the plastically deforming fibrils (red dashed line). In Figure 4e, f, the elastic and plastic patterns are clearly observable, as also demonstrated by the experimental results in Figure 4b, where the SAXD intensity plot (Figure 4b(i)) shows that all the fibrils are elastic at the yielding point (tissue strain = 0.6%), whereas for a tissue strain of 3.2% (Figure 4b(ii)) the coexistence of plastic and elastic fibrils occurs, with 58% of fibrils at $\varepsilon_f = 2.95\%$

(plastic strain), whereas the remainder fraction at $\varepsilon_f = 0.53\%$ (elastic strain).

3.2. Role of Mode II Interfaces in Cyclic Loading. A second main finding in Gupta et al.²⁰ was the existence of hysteresis at the fibrillar level. The elasto-plastic behaviors of a set of different models under cyclic loading were simulated to discover the combined effects of fibril lateral arrangement and architecture, coupled with the interface types described in the previous subsection. We found that the experimentally observed hysteresis in the cyclic loading curves occurs when staggered fibril arrangement coupled with mode I and mode II cohesive surface interfaces are introduced in cyclic simulations. In fact, the presence of only mode I or mode II interfaces for, respectively, a system of two aligned or two-column fibrils is clearly not responsible for hysteresis (Figure 5a, b). These effects do not arise from the limited number of fibrils considered: an increase in number of fibrils from two to four, in a condition of nonoverlap, results in no hysteresis with both damageable and undamageable mode II interfaces (Figure 5c₁, c₂). As fibrils do not transmit load through shearing in the configurations shown in Figures 5c₁, c₂, no difference between damageable and undamageable mode II interface is observed. From our set of simulations, we observed that only the concurrence of staggered fibril arrangement and cohesive

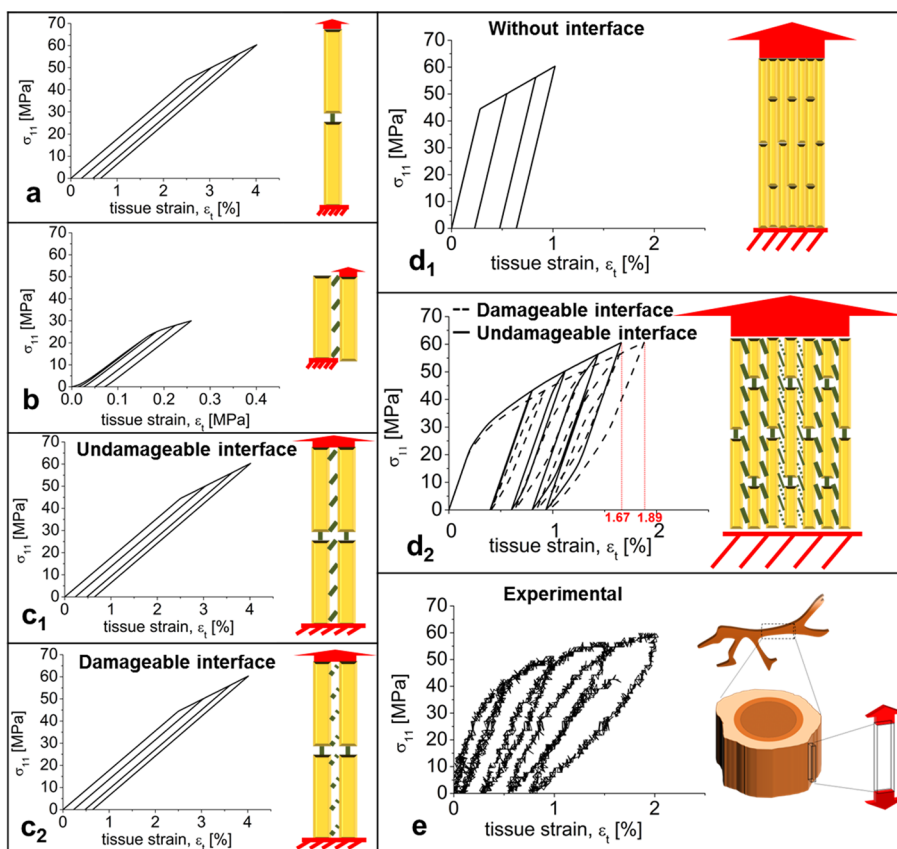


Figure 5. Cyclic loading in different fibrillar geometries: Comparisons between (a, b, c₁, c₂, d₁, d₂) numerical and (e) experimental results. (a) Two fibrils model with “mode I” non damageable interface. (b) Two fibrils model with “mode II” non damageable interfaces, in aligned configuration. (c₁) Four fibrils model with “mode I” and “mode II” non damageable interfaces, in aligned configuration. (c₂) Four fibrils model with “mode I” non damageable interface and “mode II” damageable interface, in aligned configuration. (d₁) Seven layers model without interfaces, in staggered configuration. (d₂) Comparison between two seven layers models in staggered configuration: damageable mode II interfaces at the middle layer versus undamageable ones. (e) Experimental results for cyclic loading on bone.

surface interface (not necessary damageable) leads to hysteresis in loading/unloading stress strain curves (Figure 5d₂). It can be seen from Figure 5d₁ that staggered but perfectly bonded fibrils (no cohesive interface) do not exhibit hysteresis and loading/unloading patterns perfectly overlap. The introduction of damageable mode II interfaces makes the structure more deformable. Indeed, as fibrils, in staggered configuration, transmit loading through shearing, damageable and then weaker mode II interfaces allow the whole structure to deform up to 1.89%, whereas in a condition of nondamageable interfaces, the tissue strain reaches the value of 1.67% (Figure 5d₂) at the same stress level of 60 MPa.

Numerical results for the cyclic loading curves are in very good agreement with experimental data (comparisons in Figures 5d₂, e). Maximum tissue strains, in both cases, are about 1.9% and furthermore, the structural yielding points occur at tissue strain \approx 0.22% and axial stress \approx 25 MPa, earlier than the corresponding prediction in the material law²⁰ used for simulations.

This paper shows how combination of finite elements simulations at fibrillar level, combined with experimentally derived information on ultrastructural plasticity of the fibril, enables the development of a model for the mechanical behaviors of antler bone under cyclic loading conditions, which can explain both the energy dissipation (via hysteresis) as well as the concurrent heterogeneous pattern at the nanoscale. In

addition, as shown in Figure 6, our parametric simulations allow us to conclude that the combination of:

- staggered fibrillar configuration and damageable mode II interface leads to hysteresis and fibrillar heterogeneity;
- staggered fibrillar configuration and undamageable mode II interface leads to hysteresis and fibrillar homogeneity;
- aligned fibrillar configuration and perfectly bonded boundary conditions (without cohesive behaviors) at the interfaces leads to no hysteresis and fibrillar homogeneity.

4. DISCUSSION AND CONCLUSION

Elastic deformation in bone at the nanoscale has been extensively studied^{4,32,40–42} via multiscale fiber composite models that often treat bone material as a two-scale hierarchical composite; mineralized fibrils are arranged in a staggered manner, and fibrils themselves consist of mineral platelets staggered in a collagen matrix phase. Such models are usually validated by comparing the tissue-level modulus predictions to experimentally determined stiffness, though in an ideal scenario predictions of deformation and stress at multiple levels would be calculated and compared to experiment.

In the area of structural models for inelastic and damage accumulation in bone, there are no modeling attempts for the structural response of the nanoscale bone material under cyclic loading. To fill this gap, here we proposed a model based on

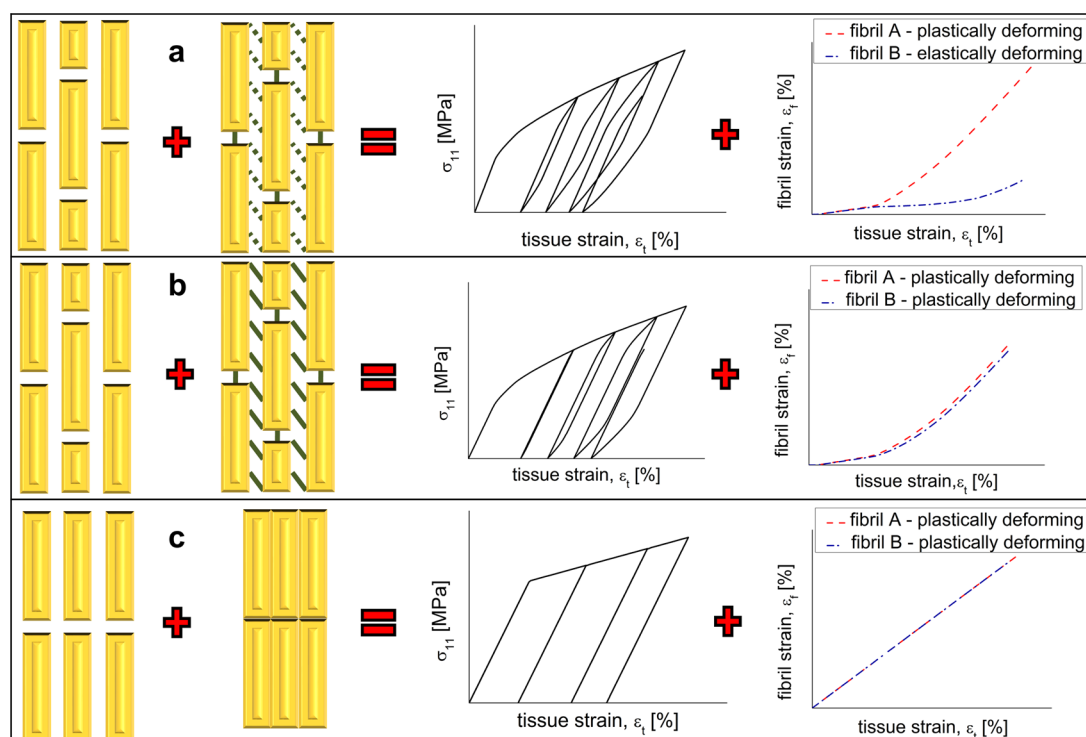


Figure 6. Summary of main results: (a) Staggered fibrillar configuration and damageable mode II interface are responsible for hysteretic stress strain curve and heterogeneous fibrillar deformation. (b) The inclusion of staggered configuration and undamageable interface leads to hysteresis and homogeneous fibril deformation. (c) Aligned fibrillar configuration and no interface lead to no hysteresis and homogeneous fibril deformation.

surface cohesive behaviors. Our main assumptions are to neglect the material properties of the interfibrillar matrix and to consider the fibrils linked by cohesive surfaces whose damage process occurs in terms of stiffness degradation. Previously, cohesive behaviors were used for studying the damage mechanisms of bone at different scales.^{43–47} Our approach, on the contrary, is based on cohesive stiffness representative of interfaces with negligible small thicknesses. The main difference between the two approaches is that in surface-based laws the damage evolution describes the degradation of the cohesive stiffness whereas in the continuum-based approach^{43–47} the damage concerns the degradation of the material stiffness. The continuum model, called also cohesive zone model, can be used to analyze both interface and bulk fracture. For example, Hamed and Jasiuk⁴³ created a multiscale model for studying the mechanisms of damage in bone and used the cohesive zone for modeling the fracture of the interface between collagen and hydroxyapatite platelets but also the fracture inside the fibrillar components. They found that the mesh size of cohesive elements had a significant effect on the strength of the mineralized fibrils. A recent study⁴⁶ investigated the evolution of damage in staggered array of mineralized collagen fibrils (MCF) embedded in extrafibrillar protein matrix modeled by continuum cohesive finite elements. The authors found that the failure mechanisms of the extrafibrillar matrix play a dominant role on the energy dissipation capacity of the system. Lin et al.⁴⁷ recently provided evidence as to the importance of the extrafibrillar matrix, considered as composite of hydroxyapatite crystals embedded in an interface modeled by cohesive finite elements, in the preyield deformation and failure mode of bone. They found that a tough interface provokes ductile deformation of matrix, as in the case of wet bone, whereas a brittle interface causes brittle deformation, as in dry bone.

Hysteresis, at higher scales in bone, has been found in experiments, but relatively few bone-specific models exist. Ascenzi et al.⁴⁸ tested single osteons and found hysteresis loops under tension. They discovered that the collagen orientation is the main factor to determine the features of hysteresis loops. In both our experimental work and in other references such as Ascenzi et al.,⁴⁸ the width of hysteretic loops tends to increase as the applied stress increases. In terms of modeling of the hysteresis loop width, the work of A. G. Evans and co-workers, who carried out modeling and numerical analysis of ceramic matrix composite deformation,⁴⁹ is relevant, although their model is applied to a different class of synthetic materials. They derived expressions for which the maximum hysteresis loop width depends on the Young's modulus of both, the fibrils and the matrix, the fibril radius and the fibril volume fraction, but also on the stress conditions, such as the maximum stress reached in the system. At lower scales an analytical model explained the inelastic response of bone,⁵⁰ indicating stress/strain hysteresis in loading/unloading tests. The authors found the shear yielding of the interface between collagen fibrils and mineral platelets to be the cause of irreversible slip and then of hysteresis. Hysteresis, in our staggered fibrillar models, is due to the presence of cohesive surface interfaces and in detail, to zones of stress concentration. In fact, we found that, once stretched or released (null surface traction applied to the structure) finite elements of the horizontally adjacent fibrils (fibrils on the same layer) are under-loaded, while finite elements of the underlying fibrils are overloaded (Figure 4c). This mechanism results in a certain delay of the structure, manifesting as hysteretic loops, necessary to reach the traction value imposed at following loading or unloading steps.

Our second finding regards heterogeneous fibrillar deformation caused by partially damageable interfaces. Heterogeneity in

the behaviors of mineralized tissue was detected as a mechanism contributing to energy dissipation.^{19,22} Mechanical properties of individual mineralized collagen have been only recently analyzed thanks to the development of innovative experimental techniques. While the fibrillar structure of collagenous tissues was explored extensively during the last decades (for a review see³⁹), only more recently have their mechanical properties been determined experimentally.^{18,51} Heterogeneity in fibrillar deformation were found in antler cortical tissue by Krauss et al.³⁴ by using a time-resolved synchrotron small-angle X-ray diffraction technique, coupled with tensile testing. They found that heterogeneity in fibrillar deformations starts after the macroscopic yielding. Hang and Barber¹⁸ performed tensile testing on individual fibrils from antler using atomic force microscopy and scanning electron microscopy. They found heterogeneous deformations in fibrils showing either yield or strain hardening. The structural mechanism for interfacial failure between fibrils may involve the breakage of sacrificial bonds in the noncollagenous proteins found in the interfibrillar matrix.²² These weak calcium mediated bonds within and between proteins such as osteopontin or osteonectin have been proposed to play a significant role in bone toughness.^{52,53} Recently, Poundarik et al.²¹ proposed a mechanism of clusters of extrafibrillar mineral held together by noncollagenous protein glue. Under deformation, this model generates an inhomogeneous strain and stress pattern at the fibrillar level. Although we found, instead, that damageable mode II interfaces are responsible for heterogeneous strain fields, the structural origin of such damage may involve mechanisms as proposed by Poundarik et al.²¹ In detail, fibrils surrounded by damageable interfaces behave elastically while other fibrils reach higher stress values after yielding (Figure 7a in Appendix 1). At lower scales, Buehler²⁵ found the existence of a range of adhesive energy values between molecules (0.01–1 J/m²), which optimizes the toughening mechanisms. Following this concept of optimization, a possible application of our model may be a quantitative and parametric approach to evaluate the types of mechanical behaviors of interfaces which lead to optimized toughness. It must be remarked that in our models, we consider damage only as stiffness degradation of cohesive surfaces and not as failure and that we use a 2D model. In terms of multiscale modeling of toughness, the current model will allow one to homogenize the properties at the fibrillar scale and these homogenized properties could be inserted into a larger-scale 3D model for the study of crack propagation and damage in real antler bone.

In conclusion, by constructing a finite element model for the inelastic cyclic loading response of mineralized collagen fibrils in antler, we show that the hysteresis observed is due to interfibrillar staggering leading to inhomogeneous stress fields along the fibril and localized intrafibrillar plasticity, whereas the inhomogeneous deformation arises from the weak interfaces between fibrils, potentially mediated by sacrificial bonds in the noncollagenous proteins between fibrils.

■ ASSOCIATED CONTENT

📄 Supporting Information

The Supporting Information is available free of charge on the ACS Publications website at DOI: 10.1021/acsbomaterials.6b00637.

Effect of damageable and undamageable interfaces on fibrillar stress distribution, and influence of different overlap values between fibrils and damage laws (PDF)

■ AUTHOR INFORMATION

Corresponding Author

*Himadri S. Gupta (h.gupta@qmul.ac.uk).

ORCID

H. S. Gupta: 0000-0003-2201-8933

Notes

The authors declare no competing financial interest.

■ ACKNOWLEDGMENTS

H.S.G. thanks Peter Fratzl and Stefanie Krauss (Max Planck Institute of Colloids and Interfaces, Potsdam, Germany), Dr. Sergio Funari (HASYLAB-DESY, beamline A2), and Prof. John Currey (University of York) for very pleasant scientific collaboration on earlier work on antler bone.^{20,34} E.B. is supported by the Queen Mary University of London Start-up grant for new academics. N.M.P. is supported by the European Research Council (ERC StG Ideas 2011 BIHSNAM n. 279985, ERC PoC 2015 SILKENE nr. 693670), and by the European Commission under the Graphene Flagship (WP14 Polymer Nanocomposites, n. 696656).

■ REFERENCES

- (1) Meyers, M. A.; Chen, P.-Y.; Lin, A. Y.-M.; Seki, Y. Biological materials: structure and mechanical properties. *Prog. Mater. Sci.* **2008**, *53* (1), 1–206.
- (2) Fratzl, P.; Weinkamer, R. Nature's hierarchical materials. *Prog. Mater. Sci.* **2007**, *52* (8), 1263–1334.
- (3) Buehler, M. J. Nano- and micromechanical properties of hierarchical biological materials and tissues. *J. Mater. Sci.* **2007**, *42* (21), 8765–8770.
- (4) Ji, B.; Gao, H. Mechanical properties of nanostructure of biological materials. *J. Mech. Phys. Solids* **2004**, *52* (9), 1963–1990.
- (5) Weiner, S.; Wagner, H. D. The material bone: structure-mechanical function relations. *Annu. Rev. Mater. Sci.* **1998**, *28* (1), 271–298.
- (6) Bonderer, L. J.; Studart, A. R.; Gauckler, L. J. Bioinspired design and assembly of platelet reinforced polymer films. *Science* **2008**, *319* (5866), 1069–1073.
- (7) Pugno, N. M. Mimicking nacre with super-nanotubes for producing optimized super-composites. *Nanotechnology* **2006**, *17* (21), 5480.
- (8) Bosia, F.; Buehler, M. J.; Pugno, N. M. Hierarchical simulations for the design of supertough nanofibers inspired by spider silk. *Phys. Rev. E* **2010**, *82* (5), 056103.
- (9) Bosia, F.; Abdalrahman, T.; Pugno, N. M. Self-healing of hierarchical materials. *Langmuir* **2014**, *30* (4), 1123–1133.
- (10) Bosia, F.; Abdalrahman, T.; Pugno, N. M. Investigating the role of hierarchy on the strength of composite materials: evidence of a crucial synergy between hierarchy and material mixing. *Nanoscale* **2012**, *4* (4), 1200–1207.
- (11) Wang, Y.; Azais, T.; Robin, M.; Vallée, A.; Catania, C.; Legriel, P.; Pehau-Arnaudet, G.; Babonneau, F.; Giraud-Guille, M.-M.; Nassif, N. The predominant role of collagen in the nucleation, growth, structure and orientation of bone apatite. *Nat. Mater.* **2012**, *11* (8), 724–733.
- (12) Dimas, L. S.; Bratzel, G. H.; Eylon, I.; Buehler, M. J. Tough composites inspired by mineralized natural materials: computation, 3D printing, and testing. *Adv. Funct. Mater.* **2013**, *23* (36), 4629–4638.
- (13) Compton, B. G.; Lewis, J. A. 3D-printing of lightweight cellular composites. *Adv. Mater.* **2014**, *26* (34), 5930–5935.

- (14) Koester, K. J.; Ager, J.; Ritchie, R. The true toughness of human cortical bone measured with realistically short cracks. *Nat. Mater.* **2008**, *7* (8), 672–677.
- (15) Fleck, C.; Eifler, D. Deformation behaviour and damage accumulation of cortical bone specimens from the equine tibia under cyclic loading. *J. Biomech.* **2003**, *36* (2), 179–189.
- (16) Nalla, R. K.; Kinney, J. H.; Ritchie, R. O. Mechanistic fracture criteria for the failure of human cortical bone. *Nat. Mater.* **2003**, *2* (3), 164–168.
- (17) Vashishth, D.; Behiri, J.; Bonfield, W. Crack growth resistance in cortical bone: concept of microcrack toughening. *J. Biomech.* **1997**, *30* (8), 763–769.
- (18) Hang, F.; Barber, A. H. Nano-mechanical properties of individual mineralized collagen fibrils from bone tissue. *J. R. Soc., Interface* **2011**, *8* (57), 500–505.
- (19) Tai, K.; Dao, M.; Suresh, S.; Palazoglu, A.; Ortiz, C. Nanoscale heterogeneity promotes energy dissipation in bone. *Nat. Mater.* **2007**, *6* (6), 454–462.
- (20) Gupta, H.; Krauss, S.; Kerschnitzki, M.; Karunaratne, A.; Dunlop, J.; Barber, A.; Boesecke, P.; Funari, S.; Fratzl, P. Intrafibrillar plasticity through mineral/collagen sliding is the dominant mechanism for the extreme toughness of antler bone. *J. Mech. Behav. Biomed. Mater.* **2013**, *28*, 366–382.
- (21) Poundarik, A. A.; Diab, T.; Sroga, G. E.; Ural, A.; Boskey, A. L.; Gundberg, C. M.; Vashishth, D. Dilatational band formation in bone. *Proc. Natl. Acad. Sci. U. S. A.* **2012**, *109* (47), 19178–19183.
- (22) Fantner, G. E.; Hassenkam, T.; Kindt, J. H.; Weaver, J. C.; Birkedal, H.; Pechenik, L.; Cutroni, J. A.; Cidade, G. A.; Stucky, G. D.; Morse, D. E.; Hansma, P. K. Sacrificial bonds and hidden length dissipate energy as mineralized fibrils separate during bone fracture. *Nat. Mater.* **2005**, *4* (8), 612–616.
- (23) Launey, M. E.; Buehler, M. J.; Ritchie, R. O. On the mechanistic origins of toughness in bone. *Annu. Rev. Mater. Res.* **2010**, *40*, 25–53.
- (24) Tai, K.; Ulm, F.-J.; Ortiz, C. Nanogranular origins of the strength of bone. *Nano Lett.* **2006**, *6* (11), 2520–2525.
- (25) Buehler, M. J. Molecular nanomechanics of nascent bone: fibrillar toughening by mineralization. *Nanotechnology* **2007**, *18* (29), 295102.
- (26) Gupta, H. S.; Wagermaier, W.; Zickler, G. A.; Raz-Ben Aroush, D.; Funari, S. S.; Roschger, P.; Wagner, H. D.; Fratzl, P. Nanoscale deformation mechanisms in bone. *Nano Lett.* **2005**, *5* (10), 2108–2111.
- (27) Zioupos, P.; Currey, J. The extent of microcracking and the morphology of microcracks in damaged bone. *J. Mater. Sci.* **1994**, *29* (4), 978–986.
- (28) Schwiedrzik, J.; Raghavan, R.; Bürki, A.; LeNader, V.; Wolfram, U.; Michler, J.; Zysset, P. In situ micropillar compression reveals superior strength and ductility but an absence of damage in lamellar bone. *Nat. Mater.* **2014**, *13* (7), 740–747.
- (29) Barthelat, F.; Rabiei, R. Toughness amplification in natural composites. *J. Mech. Phys. Solids* **2011**, *59* (4), 829–840.
- (30) Buehler, M. J.; Yung, Y. C. Deformation and failure of protein materials in physiologically extreme conditions and disease. *Nat. Mater.* **2009**, *8* (3), 175–188.
- (31) Bar-On, B.; Wagner, H. D. Mechanical model for staggered bio-structure. *J. Mech. Phys. Solids* **2011**, *59* (9), 1685–1701.
- (32) Bar-On, B.; Wagner, H. D. Structural motifs and elastic properties of hierarchical biological tissues—A review. *J. Struct. Biol.* **2013**, *183* (2), 149–164.
- (33) Xia, W.; Ruiz, L.; Pugno, N. M.; Keten, S. Critical length scales and strain localization govern the mechanical performance of multi-layer graphene assemblies. *Nanoscale* **2016**, *8* (12), 6456–6462.
- (34) Krauss, S.; Fratzl, P.; Seto, J.; Currey, J. D.; Estevez, J. A.; Funari, S. S.; Gupta, H. S. Inhomogeneous fibril stretching in antler starts after macroscopic yielding: Indication for a nanoscale toughening mechanism. *Bone* **2009**, *44* (6), 1105–1110.
- (35) Gupta, H. S.; Seto, J.; Wagermaier, W.; Zaslansky, P.; Boesecke, P.; Fratzl, P. Cooperative deformation of mineral and collagen in bone at the nanoscale. *Proc. Natl. Acad. Sci. U. S. A.* **2006**, *103* (47), 17741–17746.
- (36) Dong, X. N.; Almer, J. D.; Wang, X. Post-yield nanomechanics of human cortical bone in compression using synchrotron X-ray scattering techniques. *J. Biomech.* **2011**, *44* (4), 676–682.
- (37) Zimmermann, E. A.; Schaible, E.; Bale, H.; Barth, H. D.; Tang, S. Y.; Reichert, P.; Busse, B.; Alliston, T.; Ager, J. W.; Ritchie, R. O. Age-related changes in the plasticity and toughness of human cortical bone at multiple length scales. *Proc. Natl. Acad. Sci. U. S. A.* **2011**, *108* (35), 14416–14421.
- (38) Xu, X.-P.; Needleman, A. Numerical simulations of fast crack growth in brittle solids. *J. Mech. Phys. Solids* **1994**, *42* (9), 1397–1434.
- (39) Wess, T.; Cairns, D. Nanoarchitectures of the animal extracellular matrix: opportunities for synchrotron radiation studies on collagen and fibrillin. *J. Synchrotron Radiat.* **2005**, *12* (6), 751–757.
- (40) Hamed, E.; Lee, Y.; Jasiuk, I. Multiscale modeling of elastic properties of cortical bone. *Acta Mechanica* **2010**, *213* (1–2), 131–154.
- (41) Nikolov, S.; Raabe, D. Hierarchical modeling of the elastic properties of bone at submicron scales: the role of extrafibrillar mineralization. *Biophys. J.* **2008**, *94* (11), 4220–4232.
- (42) Jäger, I.; Fratzl, P. Mineralized collagen fibrils: a mechanical model with a staggered arrangement of mineral particles. *Biophys. J.* **2000**, *79* (4), 1737–1746.
- (43) Hamed, E.; Jasiuk, I. Multiscale damage and strength of lamellar bone modeled by cohesive finite elements. *J. Mech. Behav. Biomed. Mater.* **2013**, *28*, 94–110.
- (44) Ural, A. Prediction of Colles' fracture load in human radius using cohesive finite element modeling. *J. Biomech.* **2009**, *42* (1), 22–28.
- (45) Mischinski, S.; Ural, A. Finite element modeling of microcrack growth in cortical bone. *J. Appl. Mech.* **2011**, *78* (4), 041016.
- (46) Lai, Z. B.; Yan, C. Mechanical behaviour of staggered array of mineralised collagen fibrils in protein matrix: Effects of fibril dimensions and failure energy in protein matrix. *J. Mech. Behav. Biomed. Mater.* **2017**, *65*, 236–247.
- (47) Lin, L.; Samuel, J.; Zeng, X.; Wang, X. Contribution of extrafibrillar matrix to the mechanical behavior of bone using a novel cohesive finite element model. *J. Mech. Behav. Biomed. Mater.* **2017**, *65*, 224–235.
- (48) Ascenzi, A.; Benvenuti, A.; Mango, F.; Simili, R. Mechanical hysteresis loops from single osteons: technical devices and preliminary results. *J. Biomech.* **1985**, *18* (5), 391–398.
- (49) Vagaggini, E.; Domergue, J. M.; Evans, A. G. Relationships between hysteresis measurements and the constituent properties of ceramic matrix composites: I, theory. *J. Am. Ceram. Soc.* **1995**, *78* (10), 2709–2720.
- (50) Mercer, C.; He, M.; Wang, R.; Evans, A. Mechanisms governing the inelastic deformation of cortical bone and application to trabecular bone. *Acta Biomater.* **2006**, *2* (1), 59–68.
- (51) Shen, Z. L.; Dodge, M. R.; Kahn, H.; Ballarini, R.; Eppell, S. J. Stress-strain experiments on individual collagen fibrils. *Biophys. J.* **2008**, *95* (8), 3956–3963.
- (52) Thurner, P. J.; Chen, C. G.; Ionova-Martin, S.; Sun, L.; Harman, A.; Porter, A.; Ager, J. W.; Ritchie, R. O.; Alliston, T. Osteopontin deficiency increases bone fragility but preserves bone mass. *Bone* **2010**, *46* (6), 1564–1573.
- (53) Gupta, H. S.; Fratzl, P.; Kerschnitzki, M.; Benecke, G.; Wagermaier, W.; Kirchner, H. O. Evidence for an elementary process in bone plasticity with an activation enthalpy of 1 eV. *J. R. Soc., Interface* **2007**, *4* (13), 277–282.

1 **SUPPORTING INFORMATION**

2

3 **Staggered fibrils and damageable interfaces lead concurrently and**
4 **independently to hysteretic energy absorption and inhomogeneous**
5 **strain fields in cyclically loaded antler bone**

6 P. De Falco^a, E. Barbieri^a, N. Pugno^{a,b,c} and H. S. Gupta^{a*}

7 ^a *Queen Mary University of London, School of Engineering and Material Science, London, E1 4NS, UK*

8 ^b *Laboratory of Bio-Inspired and Graphene Nanomechanics, Department of Civil, Environmental and*
9 *Mechanical Engineering, University of Trento, Trento, Italy*

10 ^c *Center for Materials and Microsystems, Fondazione Bruno Kessler, Povo (Trento), Italy*

11 * Corresponding author: Himadri S. Gupta (h.gupta@qmul.ac.uk)

12

13 Number of pages: 3. Number of figures: 2.

14

15

16

17

18

19

20

21

22

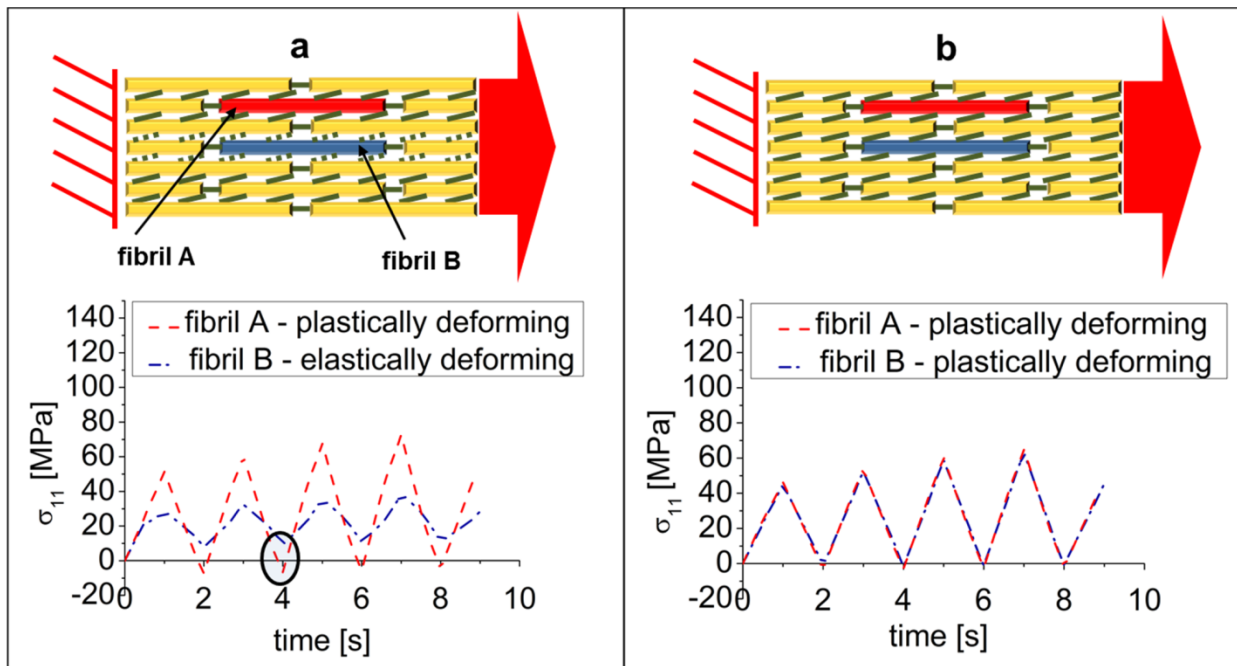
23

24

25 1 Effects of interfaces on fibrillar stress distribution

26

27 The introduction of damageable interfaces is responsible for heterogeneity and stress
28 redistribution within the staggered structure. In fact, simulations demonstrated that when
29 fibrils at the middle layer (fibrils B) are embedded in damageable shearing interfaces, their
30 capability of carrying loads reduces drastically compared with the predictions of the model
31 where the interfaces are undamageable (**Figures S1a - b**). It is also observable that at the
32 end of each unloading step, in the damageable-interfaces configuration (**Figure S1a**), fibril
33 A undergoes compression (labelled by semi-transparent circle) while fibril B remains in
34 tension. Instead, when the shearing interfaces are undamageable (**Figure S1b**), both
35 types of fibrils result unloaded at the end of each unloading steps (at seconds 2, 4, 6 and
36 8).



38

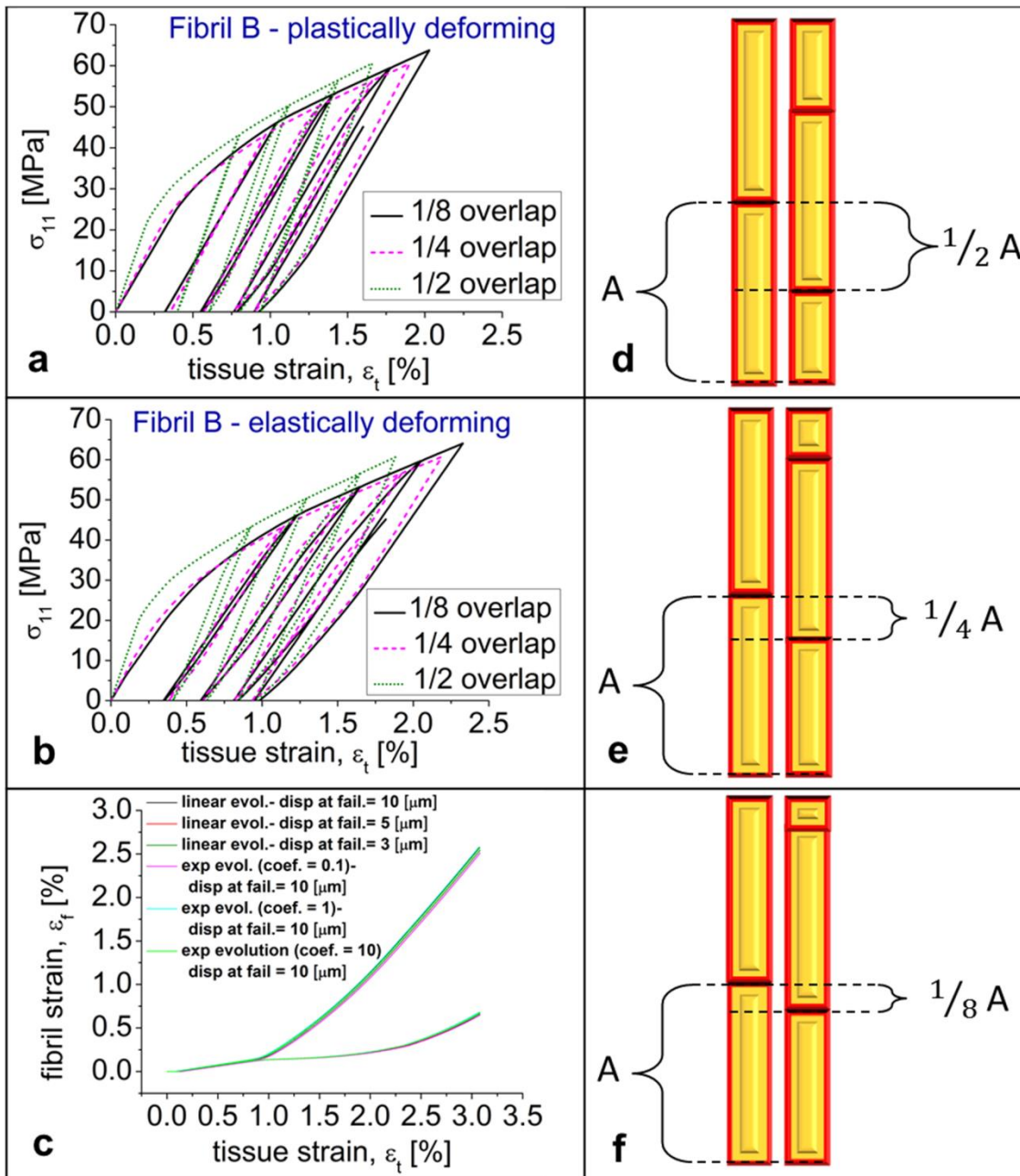
39 **Figure S1 - Numerical stress variation in time for fibril A and B, when the interfaces**
40 **surrounding the middle layer are (a) damageable or (b) undamageable.**

40

41 **2 Parametric studies of overlaps and cohesive laws**

42

43 A set of parametric simulations was performed to verify the influence of overlap between
44 fibrils in staggered configuration and the effect of different cohesive laws for the
45 damageable interfaces. Simulations prove that in both cases, with and without
46 damageable interfaces, the staggered structure becomes more deformable (**Figures S2a -**
47 **b**) as the overlap between fibrils at adjacent layers reduces from half to $1/8^{\text{th}}$ of the basic
48 fibril length (see **Figure S2f** for the representation of overlap levels). It is also interesting
49 to notice that the hysteretic loops width decreases as the overlap decreases (**Figures S2c**
50 **- d**). Furthermore, simulations show the irrelevant role of damage cohesive evolution laws
51 in the heterogeneity of the system. In fact, linear and exponential damage evolution laws
52 with different displacement at failure values were tested and very slight differences in the
53 fibrillar behaviors were found (**Figure S2e**).



54

55 **Figure S2 - Parametric simulations:** (a, b) Cyclic simulations for (a) undamageable
 56 interfaces and (b) damageable interfaces (only between the middle layer and the two
 57 adjacent ones) for different levels of overlap between fibrils at adjacent layers. (c, d)
 58 Increasing in hysteretic loop width. (e) Results for different damage evolution laws
 59 describing the damageable interfaces. (f) Levels of overlap considered for simulations.

60